






Morphologies of electric-field-driven cracks in dried dispersions of ellipsoidsMegha Emerse ¹, Hisayama ^{1,*}, Madivala G. Basavaraj ^{2,3}, Rajesh Singh ^{1,3,†} and Dillip K. Satapathy ^{1,3,‡}¹*Department of Physics, IIT Madras, Chennai 600036, India*²*PECS Laboratory, Department of Chemical Engineering, IIT Madras, Chennai 600036, India*³*Center for Soft and Biological Matter, IIT Madras, Chennai 600036, India*

(Received 29 August 2023; accepted 18 January 2024; published 14 February 2024)

We report an experimental and theoretical study of the morphology of desiccation cracks formed in deposits of hematite ellipsoids dried in an externally applied alternating current (ac) electric field. A series of transitions in the crack morphology is observed by modulating the frequency and the strength of the applied field. We also found a clear transition in the morphology of cracks as a function of the aspect ratio of the ellipsoid. We show that these transitions in the crack morphology can be explained by a linear stability analysis of the equation describing the effective dynamics of an ellipsoid placed in an externally applied ac electric field.

DOI: [10.1103/PhysRevE.109.024604](https://doi.org/10.1103/PhysRevE.109.024604)**I. INTRODUCTION**

Desiccation cracks are a ubiquitous phenomenon in nature and are encountered in a great variety of sizes and morphologies in natural settings such as dry puddles, riverbanks, and dry playas, where cycles of wetting and drying occur. Their formation is primarily associated with the evaporation of water or moisture from the surface of the material [1,2]. Desiccation cracks are also of interest in diverse scientific fields, including testing the authenticity of paintings, geology, and environmental science, as they can provide information about past environmental conditions and processes [3,4]. On the other hand, desiccation cracks are also observed in particle coating films, which play a crucial role in diverse scientific and technological applications. These films are often created by drying deposition of colloids and nanoparticle dispersions on solid surfaces. As the solvent evaporates, the film experiences shrinkage and the adhesion to the underlying solid substrate opposes this contraction, resulting in stress within the material. This interplay between drying-induced shrinkage and adhesion to the substrate gives rise to desiccation cracks [5,6]. Cracks serve to alleviate stresses locally along their sides but concentrate stress at their tips. Consequently, the crack tip propagates until the stress at the tip falls below the local tensile strength of the material. Over time, a network of cracks, often referred to as a crack pattern, forms as multiple cracks nucleate, grow, and interconnect [7,8]. While considerable knowledge was acquired regarding the nucleation, growth, dynamics, and stability of a single crack in an elastic solid, numerous questions related to the formation of crack patterns induced by stresses arising from nonequilibrium

processes like drying and cooling remain largely unanswered [9–11].

The intriguing patterns of cracks have captivated scientists and have been a subject of extensive study. Researchers have conducted well-controlled experiments in laboratory settings and theoretical simulations spanning decades to unravel the intricacies of crack formation. Skejltorp and Meakin investigated the formation and propagation of desiccation cracks in the drying process of a monolayer of uniformly sized polystyrene microspheres confined between two parallel sheets of glass [12]. Detailed investigation of desiccation crack patterns and their scaling characteristics observed in coffee-water mixtures [6], corn flour–water mixtures [13,14] and silica sols [15], and drying colloidal films [16] are reported. These cracks typically manifest with various morphologies, such as a network of polygons, as circular, linear, coiled, undulating, and starlike patterns [1,17]. The nucleation of a single desiccation crack and the crack pattern that emerges from multiple cracks in a drying colloidal film depends on various aspects such as the particle shape [18,19], nature of substrate [10], colloidal interactions [2,20], drying conditions, etc. [2,15,21].

The self-assembly of particles in a drying colloidal film can be manipulated by drying conditions, shape of the particles [22,23], and under the influence of various external fields [24]. The correlation between the arrangement of colloidal particles in a film and the occurrence of drying-induced cracks allows for the controlled modulation of crack patterns through the application of external fields. These fields encompass thermal and magnetic fields [25–27], as well as electric fields [28] and combinations of different fields such as thermomagnetic. Several studies have investigated the manipulation of crack morphology in particulate films, predominantly composed of spherical particles, through the application of magnetic, thermal, and electric fields [29–33]. Recent findings indicate that upon complete drying of dispersions containing spherical colloids, radial cracks form in the particulate film. Additionally, dispersions with elliptical particles exhibiting an aspect ratio

*Present address: Polymer and Microfluidics Group, Imperial College London, United Kingdom.

[†]rsingh@physics.iitm.ac.in

[‡]dks@iitm.ac.in

TABLE I. Quantities of different chemicals used to obtain ellipsoids of different aspect ratios in a 200 ml reaction mixture.

Aspect ratio (α)	(CONH_2) ₂ (g)	$\text{Fe}(\text{ClO}_4)_3 \cdot x\text{H}_2\text{O}$ (g)	$\text{NaH}_2\text{PO}_4 \cdot \text{H}_2\text{O}$ (g)
1.3 ± 0.1	1.2012	9.2464	0.0289
2.7 ± 0.4	1.2012	9.2464	0.05349
4.8 ± 0.5	1.2012	9.2464	0.1002

(α) greater than 2.4 result in the formation of circular cracks [18]. In films composed of anisotropic particles, the direction of cracks is influenced by the orientation of particles, which, in turn, depends on the externally applied field. While there are a few reports on the directed self-assembly of ellipsoids and transitions in particle orientation as a function of applied frequency and field strength of an ac electric field [28,34–38], the exploration of cracking patterns is relatively limited. The impact of varying the magnitude and frequency of the applied alternating current electric field on desiccation cracks in films composed of anisotropic colloidal particles with different aspect ratios and the identification of a critical frequency governing the transition in crack orientation constitute the primary objectives of this study.

In this article, we report the combined impact of frequency and strength of applied alternating current electric field on the orientation of desiccation cracks in a deposit of ellipsoids. By increasing the frequency alone, multiple transitions in the crack morphologies, such as (a) from random polygonal to linear cracks perpendicular to the electric field, (b) from linear perpendicular to nonlinear cracks, and (c) to linear cracks aligned with the electric field, were observed. A complete experimental phase diagram for crack morphology was obtained by varying the strength and frequency of the applied electric field. These observations were corroborated by taking into account the effective torque imposed on the ellipsoids by the external field and performing a linear stability analysis.

II. MATERIALS AND METHODS

A. Synthesis and characterization of ellipsoids

The hematite particles ($\alpha\text{-Fe}_2\text{O}_3$) with different aspect ratios varying from 1.3 to 4.8 were synthesized by forced hydrolysis method [39,40]. The amount of the reagents used for the synthesis of different aspect ratio (α) from a 200 mL reaction mixture is given in Table I. The HR-SEM images of hematite particles of different aspect ratios are given in Fig. 1.

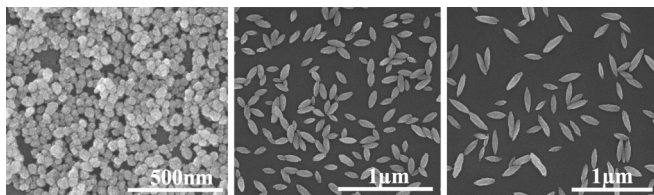


FIG. 1. Scanning electron microscopy (SEM) images of ellipsoids having different aspect ratios. The scale bar is shown in each image.

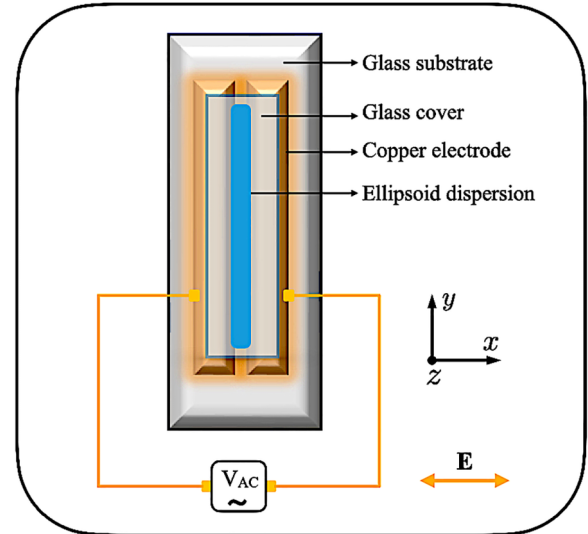


FIG. 2. Schematic of the experimental setup showing an ellipsoid dispersion placed between two parallel copper electrodes used for applying an alternating electric field \mathbf{E} , whose direction is marked. As shown in the figure, a glass cover is placed over the experimental chamber containing the ellipsoid dispersion. Direction of the applied electric field is also shown.

The aspect ratio (α) of the particles, defined as the ratio of the length of the semimajor axis to the length of the semiminor axis, is determined from the high-resolution scanning electron microscopy images (HR-SEM) using IMAGEJ software. After thorough washing of particles, the pH of the aqueous hematite particle dispersion is adjusted to 2 by adding an appropriate quantity of HNO_3 . The initial concentration of the hematite ellipsoids in the dispersion was maintained at ~ 5 wt. %. We note that the ζ potential of the hematite particles can be tuned over a wide range by varying the pH of the suspension [40,41]. At $\text{pH} = 2$, the hematite particles are highly positively charged with a ζ potential of +40 mV when measured in 0.01 mM aqueous NaCl solution. Under these conditions, the hematite particles in the dispersions are highly stable against aggregation and gravity sedimentation [40,41].

B. Experimental setup

Figure 2 shows a schematic of the experimental setup used. The glass slides, which also serve as solid substrates for drying drop experiments under the influence of electric field, were cleaned using soap, water, and acetone. Finally, the slides were washed with Milli-Q water and dried using nitrogen gas. Two strips of commercially available copper conductive adhesive tape of approximately 9.8 mm width were fixed (parallel to each other) on a clean microscopy glass slide. The distance between these copper strips, which act as electrodes, was 2 mm. The copper wire of 0.25 mm diameter cleaned with sandpaper was then pasted on the glass slide with the help of silver paste and the assembly was left undisturbed to dry. On this coplanar electrode assembly, about 10 μl dispersion of hematite ellipsoids (in the rest of the manuscript, the hematite ellipsoids are referred to as ellipsoids for brevity) was dispensed in the gap between the electrodes

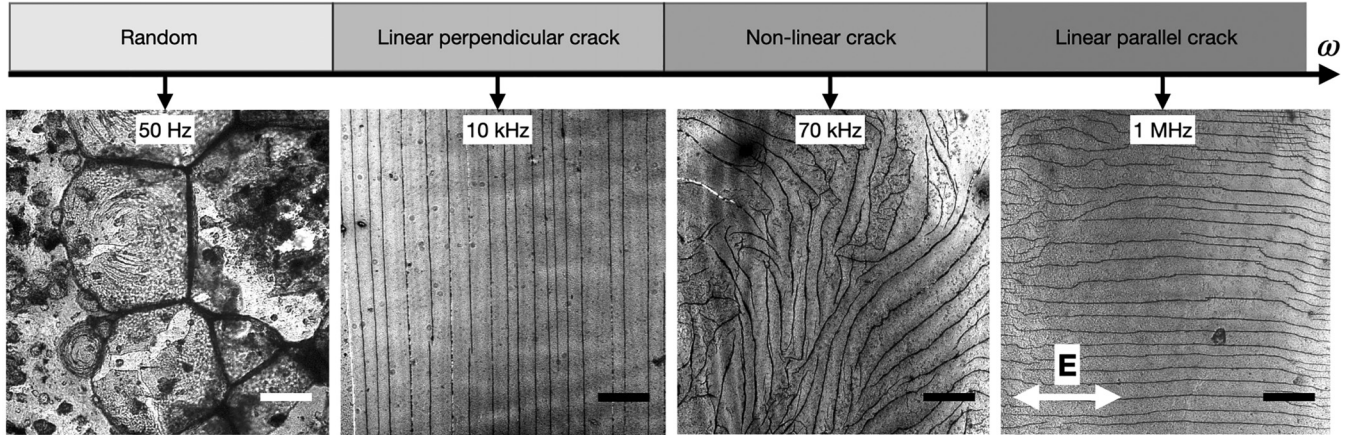


FIG. 3. Morphology of desiccation cracks as a function of the frequency (ω) of the applied ac electric field. The shaded regions highlight the transition of cracks as the frequency is varied. The aspect ratio of the ellipsoids used is $\alpha = 4.8 \pm 0.5$, while the strength of the electric field is fixed at $E_0 = 75$ kV/m. The scale bar is 100 μm .

using a micropipette. The direction of the externally applied electric field is along the x direction as shown in Fig. 2. The dispersion was observed to form a thin layer. Immediately, a glass cover slip was placed on top of the coplanar electrode assembly to confine the dispersion.

The ellipsoidal dispersion, as shown in Fig. 2, was allowed to dry in the presence of an alternating electric field applied by using a frequency generator and a voltage amplifier. A high-voltage power amplifier (Model 2340, TEGAM) and a sine wave signal from a function generator (Model WS8101, 100 MHz Tabor) were used. Multiple drying experiments, with at least three repetitions, were performed by varying the frequency of the applied field from 5 kHz to 1 MHz and the magnitude of the electric field from 450 V/cm to 1000 V/cm. All the experiments were carried out at a constant temperature of about 25 $^{\circ}\text{C}$ and at a relative humidity $33 \pm 5\%$. Finally, the dried particulate films were characterized by optical microscopy (Olympus IX71) and scanning electron microscopy.

III. RESULT AND DISCUSSIONS

A. Effect of frequency of ac electric field

The drying-induced stress energy that is accumulated in a deposit of colloids is released by the formation of desiccation cracks [16,42]. The microstructure of the cracks can be tailored by the application of external fields [25,26,28]. Here, we present a systematic study on the effect of the frequency and strength of an applied alternating current (ac) electric field on the microstructure of the particulate deposit and the resulting desiccation cracks during the evaporative self-assembly of ellipsoids.

The morphology of cracks is found to be strongly correlated with the frequency of the applied electric field. It is also observed that the crack morphology critically depends on the strength of the applied field as well as the aspect ratio of the ellipsoids. The morphology of the desiccation cracks observed in a deposit of ellipsoids with an aspect ratio of $\alpha = 4.8$, at a fixed electric field strength $E_0 = 75$ kV/m, and as a function of the frequency of the applied ac electric

field is shown in Fig. 3. At very low frequencies (less than 1 kHz), random polygonal cracks form and a representative crack pattern corresponding to 50 Hz is shown in Fig. 3. When the frequency is increased, as seen in the panel corresponding to 10 kHz, the cracks become linear and align perpendicular to the applied field. At very high frequencies, the cracks switch their orientation and become parallel to the applied field direction (see panel corresponding to 1 MHz). We note that the switch from perpendicular to parallel configuration is not abrupt but proceeds through a regime where the cracks are nonlinear and randomly oriented (see panel corresponding to 70 kHz). The detailed evolution of the crack morphology as a function of applied frequency is given in the Appendixes (Fig. 8). It is interesting to note that the transition from random polygonal to linear perpendicular crack morphology is abrupt. This transition is found to occur at a frequency between 870 and 880 Hz (see the Appendixes, Fig. 9), which is specific to the fixed electric field strength ($E_0 = 75$ kV/m), and aspect ratio of the ellipsoids ($\alpha = 4.8 \pm 0.5$) considered in this set of experiments. It is germane to note that the direction of cracks in films composed of anisotropic particles is governed by the orientation of particles (see the Appendixes Fig. 10).

B. Effect of the magnitude of ac electric field

Next, we investigate the combined effect of the strength and frequency of the ac electric field on the morphology of cracks formed in the dried deposits of ellipsoids. The strength of the electric field is varied from 45 kV/m to 100 kV/m, while the frequency is varied from 5 kHz to 1 MHz. A comprehensive phase diagram depicting the orientation and the transition of the desiccation cracks as a function of the strength and frequency of the electric field is shown in Fig. 4. As can be seen from the phase diagram, the transition of the cracks from a direction perpendicular to parallel to the electric field can be achieved either by tuning the frequency at constant field strength (highlighted by the blue-shaded region) or by changing the field strength at a constant frequency (highlighted by the green shaded region). However, it is worth mentioning that the nature of the phase diagram

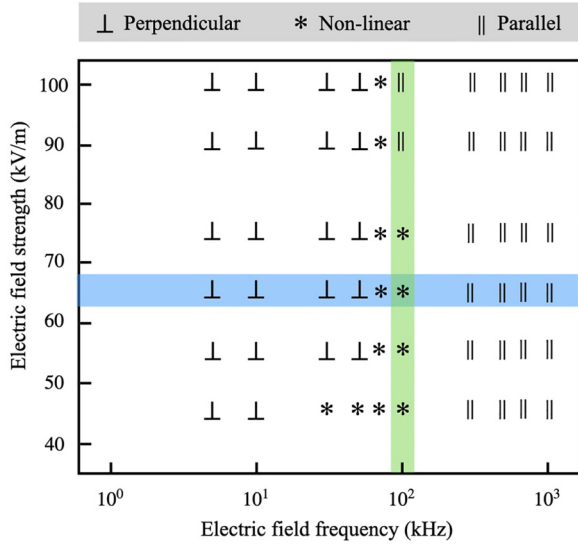


FIG. 4. Phase diagram showing crack morphology as a function of the strength of the electric field (E_0) and its frequency (ω). The shaded regions highlight the transition of cracks as the control parameters are varied. The aspect ratio of the ellipsoids is kept fixed at $\alpha = 4.8 \pm 0.5$.

may alter for ellipsoids with different aspect ratios and will be discussed later. Some of the representative crack patterns that are recorded by tuning the frequency and field strength are presented in Fig. 5.

C. Effect of aspect ratio of ellipsoids

The crack patterns shown in Figs. 3 to 5 are recorded for hematite ellipsoids having an aspect ratio $\alpha = 4.8 \pm 0.5$. In order to probe if there exists a correlation between the aspect ratio of the particles and the orientation of cracks, similar experiments with particles of different aspect ratios are performed. Aqueous dispersions containing hematite ellipsoids with aspect ratios of about 1.3 and 2.7 are dried under a

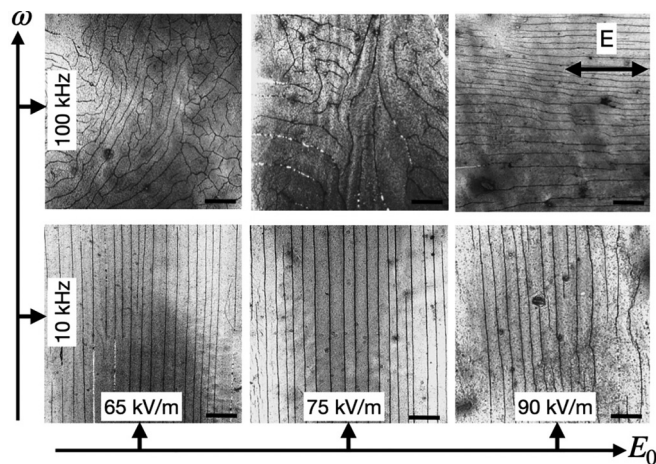


FIG. 5. Morphology of desiccation crack as a function of strength of the electric field (E_0) and its frequency (ω). This corresponds to a few representative points of the phase diagram shown in Fig. 4. The scale bar is 100 μm .

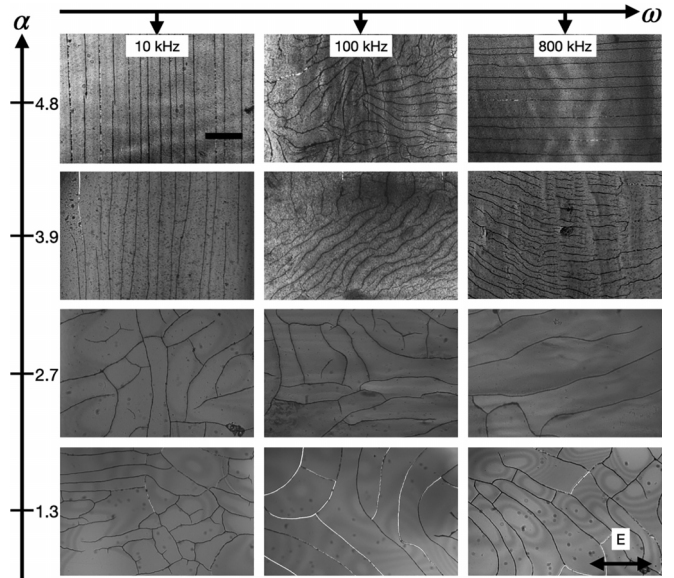


FIG. 6. Morphology of desiccation cracks as a function of the frequency of the applied ac electric field (E_0) and aspect ratio of the ellipsoids in the dispersion. The strength of the electric field is fixed at 75 kV/m. The scale bar is 100 μm .

fixed strength of the applied ac electric field with varying frequency. The resulting crack morphologies are shown in Fig. 6. The optical microscopy images reveal that nonlinear and interconnected cracks form for low aspect ratio particles ($\alpha = 1.3 \pm 0.1$). The nature of the cracks remains invariant irrespective of the strength (not shown here) and frequency of the applied electric field. The crack morphologies do not change even if we increase the aspect ratio to 2.7 ± 0.4 . It is interesting to note that on increasing the aspect ratio further to 3.9 or higher, as shown in Fig. 6, the crack orientation starts to respond to the applied ac electric field depending on its strength and frequency. As can be seen from these optical microscopy images, the cracks are perpendicular to the applied electric field for 10 kHz frequency, while they turn almost parallel at higher frequencies (such as 800 kHz). For intermediate values of frequencies, nonlinear interconnected cracks are formed, which is similar to what is observed for $\alpha = 4.8 \pm 0.5$, as discussed above.

D. Stability analysis of the ellipsoid dynamics

In this section, we rationalize the experimental results showing the critical dependence of the crack morphology on the (a) frequency, (b) strength of the applied field, and (c) aspect ratio of the particle. These explanations are obtained by a linear stability analysis of the equations that describe the dynamics of an ellipsoid in an externally applied ac electric field. To this end, we exploit the dielectric nature of the particles. A dielectric particle gets polarized under an externally applied electric field and behaves as an electric dipole. The properties of induced dipoles as a function of field strength and frequency are studied using the Maxwell-Wagner-Sillars polarization model [43–45]. In this model, the induced electric dipole depends on both the strength and the frequency of the applied ac electric field because the polarization of the

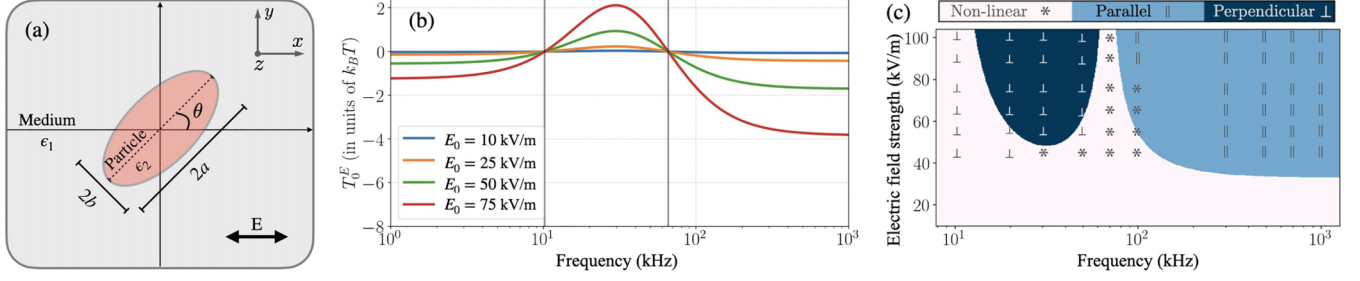


FIG. 7. (a) Schematic of an ellipsoid of permittivity ϵ_2 in an alternating electric field \mathbf{E} along \hat{x} axis in a fluid medium of permittivity ϵ_1 . The long axis of the ellipsoid of length a makes an angle θ with the \hat{x} axis. Panel (b) shows the strength of the torque T_0^E as a function of frequency, Eq. (3), for four different values of electric field strength E_0 . The vertical thick lines parallel to the torque axis indicate frequencies at which the torque changes sign. Here we have used $a = b\alpha$ nm, $b = 52$ nm, $\alpha = 4.8 \pm 0.5$, $\epsilon_1 = 80\epsilon_0$, $\epsilon_2 = 10\epsilon_0$, $\sigma_1 = 95 \mu\text{S m}^{-1}$, $\sigma_2 = 170 \mu\text{S m}^{-1}$, and $C = 10$. Panel (c) is the phase diagram in the plane of applied frequency and strength of the field at a fixed aspect ratio $\alpha = 4.8 \pm 0.5$. The color map is from theory, while symbols indicate experiments.

dielectric colloid is sensitive to the fluid-solid boundary [46,47]. An expression for the resulting torque \mathbf{T}^E experienced by these dipoles is given in Appendix B.

A schematic of a prolate ellipsoid ($a > b = c$) placed in an electric field is shown in Fig. 7(a). Here, a , b , and c represent the length of the semiaxes of the ellipsoid. We consider an electric field $\mathbf{E}(\omega, t) = \hat{x}E_0 \exp(j\omega t)$ directed along the x axis. Here ω is the frequency of the electric field in radians, t is the time, and $j = \sqrt{-1}$. The magnitude of the electric field parallel and perpendicular to the long axis of the ellipsoid is represented by E_{\parallel} and E_{\perp} , respectively. The corresponding components of the effective dipole moment \mathbf{p} , parallel and perpendicular to the long axis of the ellipsoid, are given as [47,48]

$$p_{\parallel} = 4\pi ab^2 \epsilon_1 K_{\parallel} E_{\parallel}, \quad p_{\perp} = 4\pi ab^2 \epsilon_1 K_{\perp} E_{\perp}. \quad (1)$$

Here, ϵ_1 is the dielectric permittivity of the medium, while K_{\parallel} and K_{\perp} are polarization factors parallel and perpendicular to the long axis of the ellipsoid, respectively (see Appendix B for their explicit expressions).

We now consider the dynamics of a prolate ellipsoid in xy plane under an applied electric field along the x direction. The ellipsoid makes an angle θ with the x axis. Since we are considering the orientation of the particle in the xy plane, we only need to take into account the torque along the z direction, which is denoted as $T^E(\omega, \theta)$. The dynamics of the angle θ is then given as

$$\dot{\theta} = \mu^R T^E(\omega, \theta) + \sqrt{2D_R} \xi. \quad (2)$$

Here, $\dot{\theta} = d\theta/dt$, μ^R is the rotational mobility of a prolate ellipsoid along its short axis, while $D_R = k_B T \mu^R$, k_B is the Boltzmann constant, T is the temperature, and ξ is the zero-mean, unit-variance Gaussian white noise. A derivation of the expression of the torque $T^E(\omega, \theta)$ acting on a prolate ellipsoid is given in Appendix B. The torque experienced by the ellipsoid can be expressed as

$$T^E(\omega, \theta) = T_0^E(\omega) \sin 2\theta, \quad (3a)$$

$$T_0^E(\omega) = C[\epsilon_1(L_{\parallel} - L_{\perp})E_0^2]g(\omega). \quad (3b)$$

Here, ϵ_1 is the permittivity of the medium, while L_{\parallel} and L_{\perp} are elliptic integrals defined in Appendix B. For an ellipsoidal particle with aspect ratio, $\alpha = b/a$, the L_{\parallel} and L_{\perp} are related

as $L_{\parallel} + 2L_{\perp} = 1$. We note that, for the special case of a sphere ($\alpha = 1$), we have $L_{\parallel} = L_{\perp} = 1/3$. Here C is a positive constant, which is a factor multiplied to the strength of the torque in this effective one-particle description. This constant may arise because we ignore interparticle interactions in our model and it is thus needed to compare theoretical results and experimental observations.

It is germane to note that the torque T_0^E depends critically on three quantities: (a) strength, E_0 of the applied electric field, (b) frequency, ω of the applied electric field, and (c) the aspect ratio α of the ellipsoid. A plot of T_0^E as a function of frequency for four different values of the field strength is given in Fig. 7(b). It follows from Eq. (3) that the torque decreases as the aspect ratio approaches one and vanishes exactly for $\alpha = 1$, since $L_{\parallel} = L_{\perp}$.

From Eq. (3), it is clear that the torque on the particle is zero if either of the principal axes aligns with the applied field for $\alpha \neq 1$. In other words, there are two fixed points [49] of the dynamical system at $\theta^* = 0$ and $\theta^* = \pi/2$. We now study the stability of these two fixed points by considering a small displacement $\delta\theta$, such that $\theta = \theta^* + \delta\theta$. Using Eq. (2) and neglecting Brownian motion, the dynamics of a small perturbation $\delta\theta$ about the two fixed points is given as

$$\delta\dot{\theta} = [2\mu^R T_0^E(\omega)] \delta\theta \quad \text{for } \theta^* = 0, \quad (4a)$$

$$\delta\dot{\theta} = -[2\mu^R T_0^E(\omega)] \delta\theta \quad \text{for } \theta^* = \frac{\pi}{2}. \quad (4b)$$

From Eq. (4), it is clear that for a given perturbation $\delta\theta$ about the fixed points will decay or grow depending on the sign of the $T_0^E(\omega)$. Thus $\theta^* = 0$ is stable for $T_0^E < 0$, while $\theta^* = \pi/2$ is stable for $T_0^E > 0$.

Next, the function T_0^E , defined in Eq. (3) as a function of the frequency for various field strengths of the applied electric field, is plotted in Fig. 7(b). It can be seen that the torque is negative either for small frequencies ($\omega < \omega_1$) or for larger frequencies ($\omega > \omega_2$), while it remains positive for intermediate frequencies ($\omega_1 < \omega < \omega_2$). The region corresponding to ($\omega_2 > \omega_1$) is marked clearly in Fig. 7(b) by two vertical solid lines. The explicit expressions for ω_1 and ω_2 are given in Appendix B. It is noted that, at frequencies smaller than ω_1 , thermal fluctuations dominate and preclude any preferential alignment of the ellipsoids along the applied ac electric field. Thus, for frequencies $\omega_1 < \omega < \omega_2$, the major axis of the

ellipsoids is perpendicular to the applied field, while it is parallel for $\omega > \omega_2$. This prediction, from the stability analysis, is in agreement with the experimental observations shown in Fig. 7(c). Note that the phase diagram boundaries are obtained using these conditions: (a) perpendicular for $T_0^E > k_B T$, (b) parallel for $T_0^E < k_B T$, and (c) nonlinear for $|T_0^E| < k_B T$. The symbols indicate experiments. It is not straightforward to measure the conductivity of hematite particles and the resulting dispersion. But we would like to note that these parameters used in the fitting are of the same orders of magnitude as reported in literature [50]. We note that the agreement is not exact in this effective one-particle description. Indeed, this stability analysis predicts the qualitative behavior seen in the experiments, while only providing a semiquantitative agreement with our experiments. The present theoretical analysis can be extended by accounting for the many-body electrohydrodynamic interactions between the ellipsoids, which is an exciting direction for future work.

IV. SUMMARY

To summarize, we studied the combined effects of the frequency and strength of an applied electric field on the orientation of desiccation cracks formed on a deposit of ellipsoids. The effect of the aspect ratio of ellipsoids on the morphology of the cracks has also been investigated in detail. Multiple transitions in the morphology of the

cracks—(a) from random polygonal to linear cracks along the direction perpendicular to the applied electric field, (b) linear perpendicular to nonlinear cracks, and finally (c) linear cracks aligned along the direction of the applied electric field—are observed solely by increasing the frequency of the applied electric field. A complete phase diagram of the crack morphology by varying the strength and the frequency of the applied electric field has been obtained experimentally. We have also shown that the transitions between different crack morphologies are observed for ellipsoids having aspect ratio $\alpha \geq 3.9$. These observations have been rationalized by computing the effective torque acting on an ellipsoid in an electric field. Using linear stability analysis, we predict the transitions of the crack morphology as a function of the frequency and strength of the applied field, as well as the aspect ratio of the ellipsoids. These predictions are in agreement with the experimental observations.

ACKNOWLEDGMENTS

We thank S. Khawas for the help during the initial phase of the experiments. We thank Ignacio Pagonabarraga for the useful discussions. The generous financial support from IIT Madras under the Institutes of Eminence (IoE) scheme funded by the Ministry of Education, Government of India, is acknowledged.

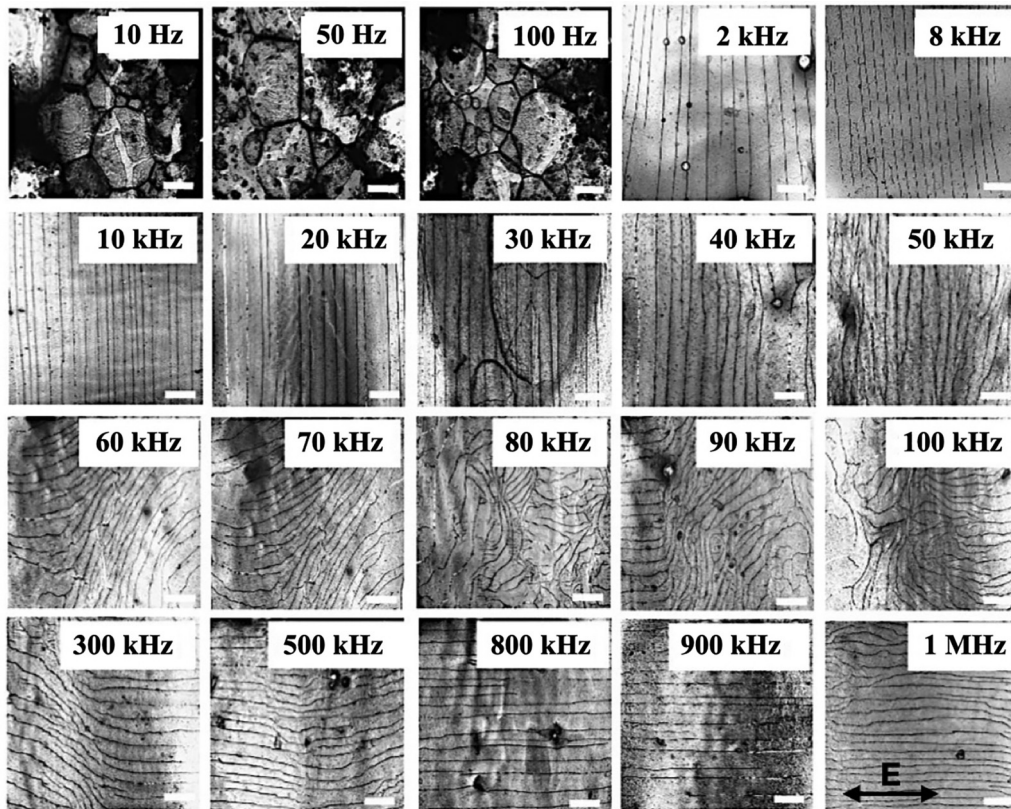


FIG. 8. The optical microscopy images showing the crack patterns recorded on the particulate film deposited between two parallel copper electrodes. The aspect ratio of the ellipsoids used for this experiment is 4.8 ± 0.5 . The strength of the applied ac electric field is 750 V/cm, and the frequency of the applied field is increased from 10 Hz up to 1 MHz. The direction of the applied electric field is marked in the figure. The scale bar is 100 μm .

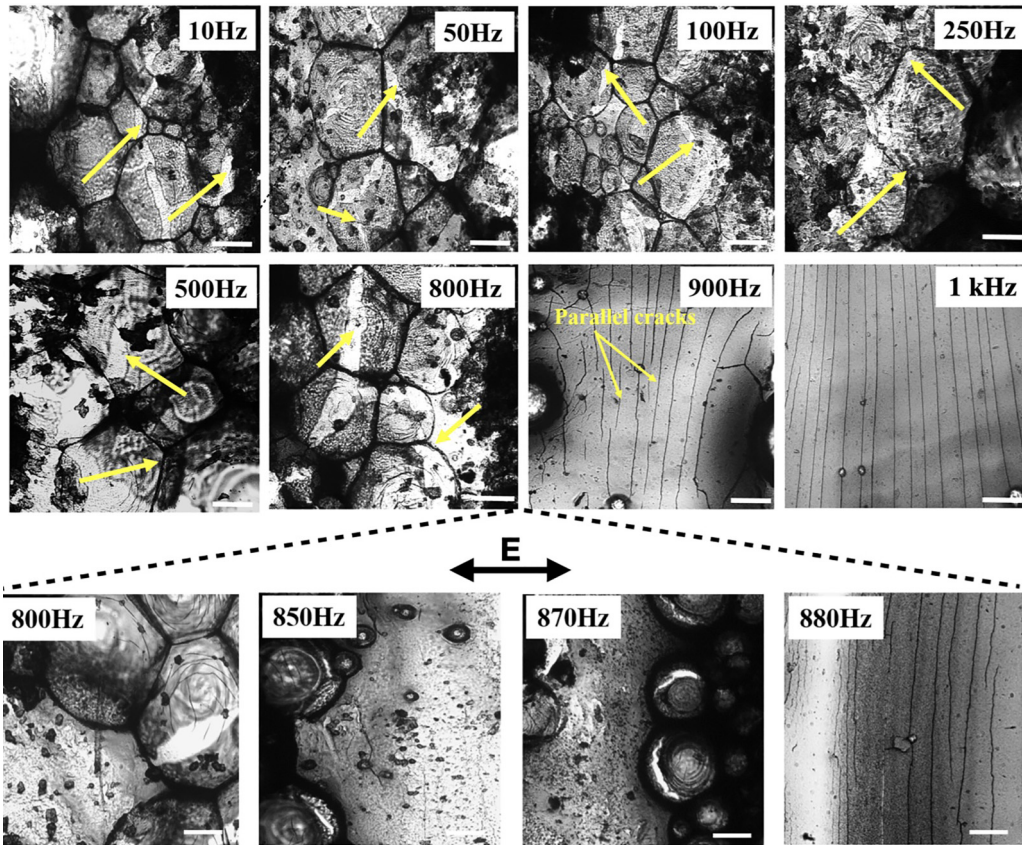


FIG. 9. Optical microscopy images of desiccation crack patterns on the particulate film for the aspect ratio 4.8 ± 0.5 . The strength of the electric field is $E = 750 \text{ V/cm}$, and the frequency is varied from 10 Hz to 1 kHz. These are the images for frequencies below 1 kHz, from which we identified the critical frequency to be 900 Hz. The frequency of the ac electric field is fine-tuned between 800 Hz and 880 Hz, revealing the critical frequency. The direction of the applied electric field is marked in the figure. The scale bar is $100 \mu\text{m}$.

APPENDIX A: CRITICAL FIELD

In Fig. 8, we show the morphology of the desiccation cracks as a function of the applied frequency of the electric field. There is a clear transition from polygonal to linear cracks between 100 Hz and 2 kHz. To explore this in detail, more experiments were performed. These are shown in Fig. 9. In this figure, we show that polygonal desiccation cracks form when the ellipsoids are dried in frequencies up to 800 Hz. As can be inferred from Fig. 9, at 900 Hz the cracks are oriented perpendicular to the direction of the electric applied field. In order to determine the critical frequency with more accuracy, further experiments were carried out by varying the frequency in the range of 800–900 Hz. As can be seen, at a critical frequency of 880 Hz a sharp random-to-oriented crack morphology is observed. Therefore, we infer that this frequency serves as the critical frequency for the electric field of strength $E = 750 \text{ V/cm}$. The yellow lines given in Fig. 9 denote the cracks which are oriented in different directions. From 900 Hz onwards the cracks become perpendicular to the applied field direction and parallel to each other.

APPENDIX B: TORQUE ON A PROLATE ELLIPSOID IN AN AC ELECTRIC FIELD

In this section, we derive an explicit expression for aligning torque acting on a nonspherical dielectric particle in an external electric field \mathbf{E} [47]. A dielectric particle induces an effective dipole moment \mathbf{p} of the ellipsoidal particle that follows from the applied field. The alignment torque is given as [47,48]

$$\mathbf{T}^E = \frac{C}{2} \text{Re}[\mathbf{p} \times \mathbf{E}^\dagger]. \quad (\text{B1})$$

Here, $\text{Re}[\dots]$ denotes the real part of the complex expression inside the bracket and \mathbf{E}^\dagger indicates the complex conjugate of the electric field, while C is a constant and positive factor, which accounts for the effective torque of the particle due to mutual hydrodynamic interactions between the particles. We choose $C = 10$ to fit experimental data. $\mu^R = \mu_0^R [-6e + 3(1 + e^2)\tilde{e}] / [4e^3(2 - e^2)]$ is the rotational mobility of a prolate ellipsoid along its short axis, where $\mu_0^R = 1/8\pi\eta a^3$, $e = [1 - (b/a)^2]^{1/2}$, and $\tilde{e} = \ln[(1 + e)/(1 - e)]$.

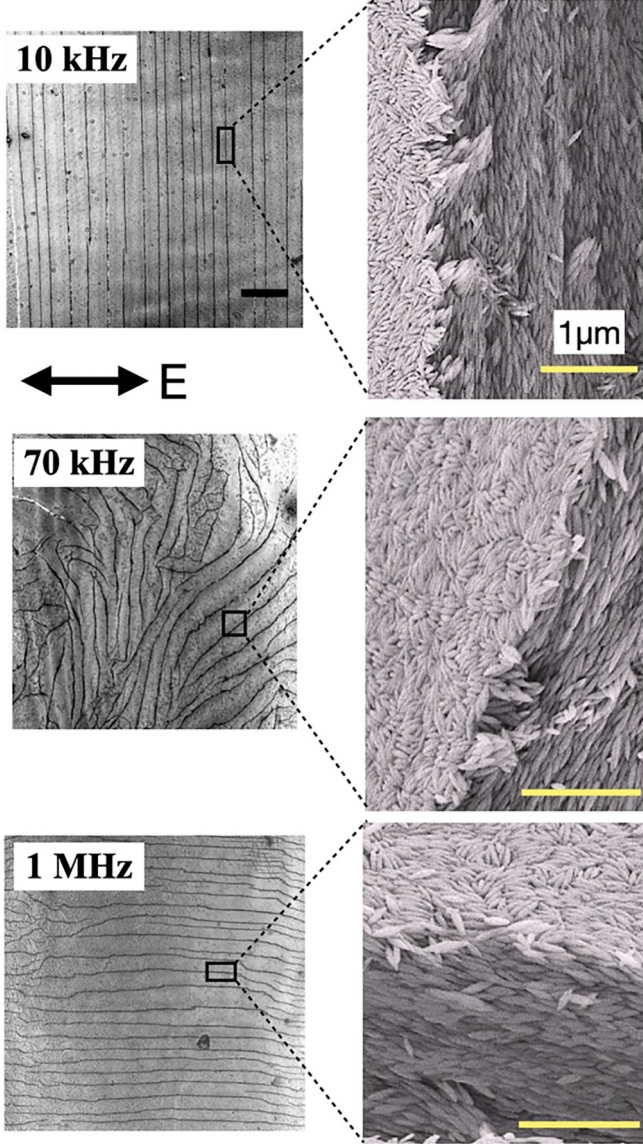


FIG. 10. (Left panel) Optical microscopy images of the desiccation cracks on the surface of particulate film containing ellipsoids of aspect ratio 4.8 ± 0.5 . The ellipsoid dispersion is dried under the application of an external ac electric of different frequencies, 10 kHz, 70 kHz, and 1 MHz, and the same strength. (Right panel) High-resolution SEM images showing the orientation of the hematite ellipsoids at the surface and inside a desiccation crack. The major axis of the ellipsoid is found to be predominantly orientated along the crack direction in the inner walls of the cracks. The scale bar for the optical microscopy images is $100 \mu\text{m}$.

The effective dipole moment \mathbf{p} of the ellipsoidal particle can be decomposed into components parallel and perpendicular to the long axis such that

$$p_{\parallel} = 4\pi ab^2 \epsilon_1 K_{\parallel} E_{\parallel}, \quad p_{\perp} = 4\pi ab^2 \epsilon_1 K_{\perp} E_{\perp}. \quad (\text{B2})$$

Here, ϵ_1 is the dielectric permittivity of the medium. We have also defined polarization factors K_{\parallel} parallel and K_{\perp} perpen-

dicular to the long axis of the ellipsoid. They are given as [47]

$$K_{\parallel}(\omega) = \frac{\epsilon}{3[\epsilon_1 + \epsilon L_{\parallel}]}, \quad K_{\perp}(\omega) = \frac{\epsilon}{3[\epsilon_1 + \epsilon L_{\perp}]}, \quad (\text{B3})$$

where $\epsilon = (\epsilon_2 - \epsilon_1)$. Here the underbar implies that the quantity is a complex number and it is dependent on the frequency of the electric field, such that $\epsilon_2 = \epsilon_2 - j\sigma_2/\omega$, where $j = \sqrt{-1}$ and ω is frequency in radians/s. The factor L_{\parallel} is given as [47]

$$L_{\parallel} = \frac{ab^2}{2} \int_0^{\infty} \frac{d\rho}{(\rho + a^2)^{3/2}(\rho + b^2)} = \frac{b^2}{2a^2 e^3} [\tilde{e} - 2e]. \quad (\text{B4})$$

The factor $L_{\perp} = \frac{1}{2}(1 - L_{\parallel})$ by definition. In the above, we have defined

$$e = \sqrt{1 - \left(\frac{b}{a}\right)^2}, \quad \tilde{e} = \ln\left(\frac{1+e}{1-e}\right). \quad (\text{B5})$$

The final expression of the strength for torque is then given by Eq. (3). It should be noted that the torque is in the \hat{z} direction. The full expression of the torque T^E is

$$T_E = Cg(\omega) [\epsilon_1(L_{\parallel} - L_{\perp})E_{\parallel}E_{\perp}] \sin 2\theta. \quad (\text{B6})$$

Here, we have defined the frequency-dependent part as

$$g(\omega) = \frac{\pi ab^2}{3} \text{Re}[K_{\parallel}(\omega)K_{\perp}(\omega)], \quad (\text{B7})$$

where $\text{Re}[\dots]$ denotes the real part of the complex expression inside the bracket. The numerator of the real part, $g(\omega)$, has the form

$$\begin{aligned} g(\omega) &= \Psi\omega^4 - \Upsilon\omega^2 + 1, \\ \Psi &= \Lambda^2 \Lambda_{\parallel} \Lambda_{\perp}, \\ \Upsilon &= \Lambda^2 + 2\Lambda_{\parallel} \Lambda_{\perp} - 2\Lambda(\Lambda_{\parallel} + \Lambda_{\perp}). \end{aligned} \quad (\text{B8})$$

Here, we have defined the following quantities:

$$\Lambda = \frac{\epsilon}{\sigma}, \quad \Lambda_{\parallel} = \frac{\epsilon_1 + \epsilon L_{\parallel}}{\sigma_1 + \sigma L_{\parallel}}, \quad \Lambda_{\perp} = \frac{\epsilon_1 + \epsilon L_{\perp}}{\sigma_1 + \sigma L_{\perp}}. \quad (\text{B9})$$

In the above, we have used $\sigma = \sigma_2 - \sigma_1$ and $\epsilon = \epsilon_2 - \epsilon_1$. In our system $\sigma_2 > \sigma_1$, while $\epsilon_1 > \epsilon_2$. Thus it follows that there are two distinct roots of Eq. (B6) for $\alpha \neq 1$. In other words, there are two values of frequency ω at which the torque goes to zero. These are

$$\omega_{1,2} = \left(\frac{\Upsilon \pm \sqrt{\Upsilon^2 - 4\Psi}}{2\Psi} \right)^{1/2}. \quad (\text{B10})$$

The above two roots have been shown in Fig. 7. The torque is negative for $\omega > \omega_2$ and $\omega < \omega_1$. For intermediate frequencies, $\omega_1 < \omega < \omega_2$, the torque is positive. Thus, from Eq. (4), it follows that the ellipsoids prefer alignment parallel to the field at high frequencies and perpendicular to the field at intermediate frequencies. At low frequencies, the strength of the torque is weaker compared to the Brownian reorientations and thus the ellipsoidal particles do not align either along or perpendicular to the direction of the applied electric field.

- [1] L. Goehring, A. Nakahara, T. Dutta, S. Tarafdar, and S. Kitsunozaki, *Desiccation Cracks and Their Patterns: Formation and Modelling in Science and Nature* (John Wiley & Sons, New York, 2015).
- [2] A. F. Routh, *Rep. Prog. Phys.* **76**, 046603 (2013).
- [3] F. Giorgiutti-Dauphiné and L. Pauchard, *J. Appl. Phys.* **120**, 065107 (2016).
- [4] R. Chen, W. Lindqwister, F. Wu, B. Mielniczuk, T. Hueckel, and M. Veveakis, *Geomech. Energy Environ.* **35**, 100488 (2023).
- [5] M. A. Biot, *J. Appl. Phys.* **12**, 155 (1941).
- [6] A. Groisman and E. Kaplan, *Europhys. Lett.* **25**, 415 (1994).
- [7] L. B. Freund, *Dynamic Fracture Mechanics* (Cambridge University Press, Cambridge, UK, 1998).
- [8] K. A. Shorlin, J. R. de Bruyn, M. Graham, and S. W. Morris, *Phys. Rev. E* **61**, 6950 (2000).
- [9] L. Goehring, L. Mahadevan, and S. W. Morris, *Proc. Natl. Acad. Sci. USA* **106**, 387 (2009).
- [10] H. Lama, T. Gogoi, M. G. Basavaraj, L. Pauchard, and D. K. Satapathy, *Phys. Rev. E* **103**, 032602 (2021).
- [11] Z. Niu, H. Gao, M. Doi, J. Zhou, and Y. Xu, *Langmuir* **38**, 13880 (2022).
- [12] A. Skjeltorp and P. Meakin, *Nature (London)* **335**, 424 (1988).
- [13] L. Goehring, A study of 3D crack patterns and columnar jointing in corn starch, Ph.D. thesis, University of Toronto, 2003.
- [14] X. Ma, J. Lowensohn, and J. C. Burton, *Phys. Rev. E* **99**, 012802 (2019).
- [15] L. Pauchard, F. Parisse, and C. Allain, *Phys. Rev. E* **59**, 3737 (1999).
- [16] K. B. Singh and M. S. Tirumkudulu, *Phys. Rev. Lett.* **98**, 218302 (2007).
- [17] V. Lazarus and L. Pauchard, *Soft Matter* **7**, 2552 (2011).
- [18] V. R. Dugyala, H. Lama, D. K. Satapathy, and M. G. Basavaraj, *Sci. Rep.* **6**, 30708 (2016).
- [19] K. Piroird, V. Lazarus, G. Gauthier, A. Lesaine, D. Bonamy, and C. Rountree, *Europhys. Lett.* **113**, 38002 (2016).
- [20] S. Kumar, M. G. Basavaraj, and D. K. Satapathy, *Langmuir* **39**, 10249 (2023).
- [21] J. Richardi, A. T. Ngo, and M. P. Pileni, *J. Phys. Chem. C* **114**, 17324 (2010).
- [22] P. J. Yunker, T. Still, M. A. Lohr, and A. Yodh, *Nature (London)* **476**, 308 (2011).
- [23] P. J. Yunker, M. A. Lohr, T. Still, A. Borodin, D. J. Durian, and A. G. Yodh, *Phys. Rev. Lett.* **110**, 035501 (2013).
- [24] A. A. Harraq, B. D. Choudhury, and B. Bharti, *Langmuir* **38**, 3001 (2022).
- [25] H. Lama, V. R. Dugyala, M. G. Basavaraj, and D. K. Satapathy, *Phys. Rev. E* **94**, 012618 (2016).
- [26] L. Pauchard, F. Elias, P. Boltenhagen, A. Cebers, and J. C. Bacri, *Phys. Rev. E* **77**, 021402 (2008).
- [27] H. Lama, R. Mondal, M. G. Basavaraj, and D. K. Satapathy, *J. Colloid Interface Sci.* **510**, 172 (2018).
- [28] M. Mittal and E. M. Furst, *Adv. Funct. Mater.* **19**, 3271 (2009).
- [29] H. Lama, M. G. Basavaraj, and D. K. Satapathy, *Soft Matter* **13**, 5445 (2017).
- [30] D. Mal, S. Sinha, T. Middy, and S. Tarafdar, *Appl. Clay Sci.* **39**, 106 (2008).
- [31] S. Nöjd, P. S. Mohanty, P. Bagheri, A. Yethiraj, and P. Schurtenberger, *Soft Matter* **9**, 9199 (2013).
- [32] M. Mittal, P. P. Lele, E. W. Kaler, and E. M. Furst, *J. Chem. Phys.* **129**, 064513 (2008).
- [33] T. Khatun, M. D. Choudhury, T. Dutta, and S. Tarafdar, *Phys. Rev. E* **86**, 016114 (2012).
- [34] P. J. Beltramo, D. Schneider, G. Fytas, and E. M. Furst, *Phys. Rev. Lett.* **113**, 205503 (2014).
- [35] H. Kim, A. Gueddida, Z. Wang, B. Djafari-Rouhani, G. Fytas, and E. M. Furst, *ACS Nano* **17**, 19224 (2023).
- [36] J. D. Forster, J.-G. Park, M. Mittal, H. Noh, C. F. Schreck, C. S. O'Hern, H. Cao, E. M. Furst, and E. R. Dufresne, *ACS Nano* **5**, 6695 (2011).
- [37] B. Esel'son, V. Ivantsov, G. Mikhailov, and R. Shchervachenko, *Sov. J. Low Temp. Phys. (Engl. Transl.) (U.S.)* **1** (1975).
- [38] J. P. Singh, P. P. Lele, F. Nettesheim, N. J. Wagner, and E. M. Furst, *Phys. Rev. E* **79**, 050401(R) (2009).
- [39] M. Ocaña, M. Morales, and C. Serna, *J. Colloid Interface Sci.* **212**, 317 (1999).
- [40] V. R. Dugyala and M. G. Basavaraj, *Langmuir* **30**, 8680 (2014).
- [41] R. Mondal, S. Semwal, P. L. Kumar, S. P. Thampi, and M. G. Basavaraj, *Langmuir* **34**, 11473 (2018).
- [42] W. P. Lee and A. F. Routh, *Langmuir* **20**, 9885 (2004).
- [43] J. C. Maxwell, *A Treatise on Electricity and Magnetism* (Clarendon Press, Oxford, 1892), Vol. 1.
- [44] K. W. Wagner, *Arch. Elektrotech.* **2**, 371 (1914).
- [45] R. W. Sillars, *Inst. Electr. Eng.-Proc. Wireless Sec. Inst.* **12**, 139 (1937).
- [46] M. Samet, V. Levchenko, G. Boiteux, G. Seytre, A. Kallel, and A. Serghei, *J. Chem. Phys.* **142**, 194703 (2015).
- [47] T. B. Jones, *Electromechanics of Particles* (Cambridge University Press, Cambridge, UK, 1995).
- [48] K. Asami, *Prog. Polym. Sci.* **27**, 1617 (2002).
- [49] S. H. Strogatz, *Nonlinear Dynamics and Chaos: With Applications to Physics, Biology, Chemistry, and Engineering* (Addison-Wesley, Redwood City, CA, 1994).
- [50] K. Supattarasakda, K. Petcharoen, T. Permpool, A. Sirivat, and W. Lerdwijitjarud, *Powder Technol.* **249**, 353 (2013).